BNL-221405-2021-TECH
C-A/AP/643

Study of Ion Generation by a ps-laser for External Injection into Electron Beam Ion Source

S. Kondrashev

May 2021

Collider Accelerator Department
Brookhaven National Laboratory

U.S. Department of Energy
USDOE Office of Science (SC), Nuclear Physics (NP) (SC-26)

DISCLAIMER

Study of Ion Generation by a ps-laser for External Injection into Electron Beam Ion Source

S. Kondrashev[1, a)], E. Beebe[1], T. Kanesue[1], M. Okamura[1], and R. Scott[2]

[1]*Brookhaven National Laboratory, Upton, NY 11973, USA*
[2]*Argonne National Laboratory, Argonne, IL 60439, USA*

[a)]Corresponding author: skondrashev@bnl.gov

We investigated ion generation from Al, Ti, Cu, Nb and Ta target elements by a picosecond-laser in the range of $10^{11} – 10^{13}$ W/cm^2 power densities at the target surface. A ps-laser with 1.27 mJ maximum energy within a 8 ps pulse and repetition rate up to 400 Hz has been used to generate a laser-ablated plasma. Dependencies of ion current vs time, total charge of registered ions as well as ion kinetic energy distributions are characterized using a Faraday cup. Significant difference in ion current dynamics between first, second and following shots onto the same target spot was found for all five target elements. The total charge of ions registered by the Faraday cup increase linearly with increasing laser pulse energy and are almost independent on the target element and number of shots onto the same target spot for all five target elements studied. Target craters have been examined using a commercially available microscope (Nikon Eclipse LV150) and crater cross section areas were found to be in the range of 0.0076 – 0.0172 mm^2 within the first five shots onto the same target spot for different target elements. A linear dependence of crater cross section square on laser pulse energy has been observed for the Ta target. Ion energy distributions for all target elements have a plateau or a slight peak in the energy range of 10 - 100 eV and long low-intensity energy tail up to tens of keV.

I. INTRODUCTION

Laser-produced plasma is created when an intense laser beam is focused onto the surface of a solid-state target. It has been studied intensively for more than fifty years since high output power lasers became available for scientific research in the mid 1960s. Many sophisticated mechanisms and phenomena involved in laser beam interaction with solids and plasmas and the subsequent hydrodynamics of the plasma expansion have been investigated and understood since that time for an extremely wide range of laser power densities between 10^8 W/cm^2 to 10^{21} W/cm^2 [1, 2].

Multiple theoretical models and numerical codes have been developed to describe and predict laser-produced plasma parameters for different target irradiation conditions in the near and far zones from the target surface [3, 4]. Initially, all experiments were carried out using nanosecond-lasers and later the research area was expanded to picocsecond-lasers (in 1980s) and femtosecond-lasers (in 1990s), as short pulse lasers became more and more available for research. Because of their unique properties, laser-produced plasma and laser ablation of solids have found numerous applications, such as intense pulsed source of highly charged ions [5, 6], sources of extreme ultraviolet (EUV) light for nanolithography [7], laser-induced breakdown spectroscopy [8], pulsed laser deposition of thin films [9], and micromachining [10].

Powerful (~5 mJ/pulse) ps-lasers with high repetition-rates (~10 kHz) have become available recently with reasonable cost, primarily for micromachining applications. Such lasers may offer significant advantages compared to ns-lasers by permitting generation nearly continuous beams of low charged ions. Intense and nearly continuous ion beam injectors combine the advantages of a pulsed laser ion source with a dc operation mode, and can find a wide range of applications, including: high dose ion implantation and surface modification [11], high flux neutron generation [12], and external injection of singly charged ions into an Electron Beam Ion Source (EBIS) [13]. Another advantage of ps-lasers is a potentially higher utilization efficiency of the target material consumed. Efficiency of target material consumption is defined here as a ratio of the total number of ions extracted from laser-ablated plasma to the total number of atoms ablated from the target within single laser pulse. The mechanism of solid target laser ablation in the picosecond range differs qualitatively from that in the nanosecond range [14]. The influence of heat conductivity on the solid target is almost negligible in the case of ps-laser ablation for laser pulse duration less than 10 ps. On the contrary, ns-laser ablation is dominated by heat conductivity. Consequently, the total number of atoms ablated from the target per laser pulse is significantly lower in the case of the ps-laser, and the utilization efficiency of target material consumption can be higher. Ion source vacuum conditions driven by ps-laser in high rep-rate mode should be better, since a much lower gas load per laser pulse is expected.

There is some experimental data on ion generation by ps-lasers available in literature for laser power densities at the target surface around and below 10^{13} W/cm^2 [15, 16] which is of the interest for injectors of low charge state ions. However, there is no comprehensive data on ion yields for different elements and target irradiation conditions. The main goal of this work is to measure ion

yields and to evaluate ion energy distributions generated by a ps-laser, for different target elements and target irradiation conditions, for the range of power densities at the target surface of 10^{11} – 10^{13} W/cm^2.

II. EXPERIMENTAL SETUP

A 3D model of target irradiation and the diagnostics chamber specifically designed and built for ion yield measurements is shown in Fig. 1.

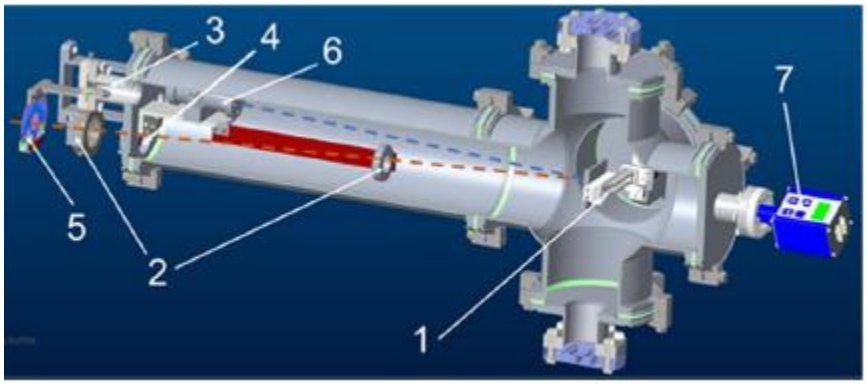

FIG. 1. 3D model of the target irradiation and diagnostics chamber: 1—3D target positioner, 2—focusing lens holders, 3—CCD camera, 4—laser input window, 5—fast laser beam shutter, 6—Faraday cup, and 7—vacuum gauge. The laser path is shown by the orange dashed line and the plasma expansion axis is indicated by the blue dashed line.

We have used a ps-laser, which is available at Argonne National Laboratory (ANL) and was previously employed for material ablation into an ECR ion source [17]. This laser is commercially available from Passat Inc. and has the following parameters: wavelength—1064 nm, pulse width—8 ps, pulse energy—up to 5 mJ/pulse, repetition rate—up to 400 Hz. The maximum average laser pulse energy of this laser at the time of our experiment was found to be 1.27 mJ with standard deviation 0.06 mJ in a single pulse mode for all measurements described below. A laser beam with diameter of about 10 mm has been focused onto the target surface by lens with 300 mm focal distance mounted inside vacuum chamber. Irradiation angle between laser beam axis and the target normal was equal to 3º. A Faraday cup (FC) with input aperture of 10 mm is placed normally to the target at 57 cm distance and it is equipped with a highly transparent meshed electrode which can be biased up to –1 kV for ion extraction from plasma and for suppression of secondary electrons from the cup. A turbomolecular pump with a 450 l/s pumping speed is attached to the

chamber to maintain the residual gas pressure inside the chamber at about $2 \cdot 10^{-7}$ Torr. An externally mounted CCD camera (Fosmon USB 6 LED webcam) allows monitoring of the laser spot position at the target surface, with observations made through a vacuum window. We use 3 ultra-high vacuum, high precision (±50 nanometer), long travel linear PPS-20 piezo positioner stages (MICRONIX USA) for 3D target positioning. It provides a 51 mm travel range in the horizontal and vertical directions and a 26 mm travel range in the lens focal depth direction. Five metal targets (Al, Ti, Cu, Nb, and Ta), each with dimensions 10 mm by 50 mm, were mounted on the target holder, which was attached to the 3D target positioner, as shown in Fig. 2.

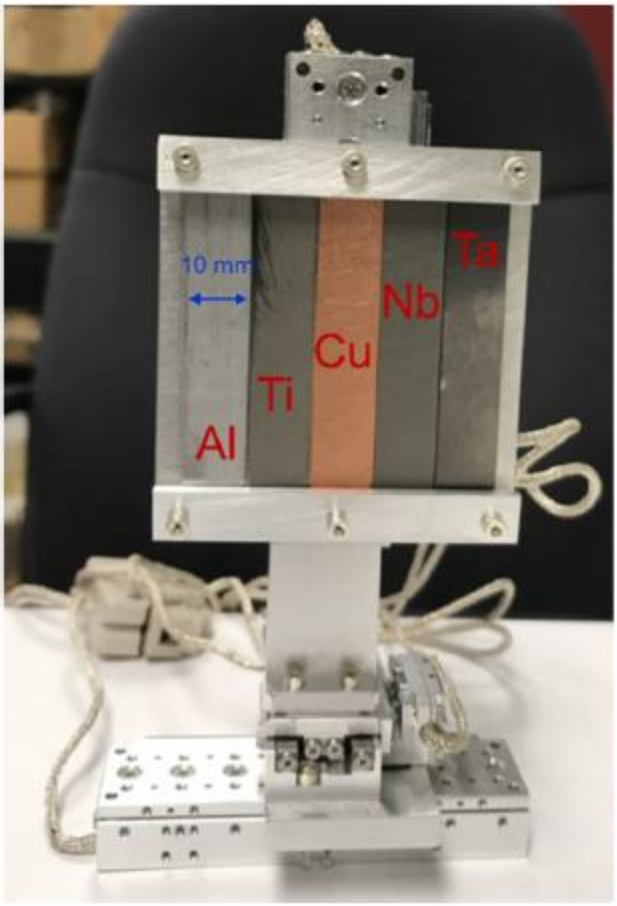

FIG. 2. Five different metal target elements mounted on a 3D target positioner.

The variation of distance between the focusing lens and the target surface caused by target translation were measured using a laser displacement sensor over the whole range of horizontal

and vertical translation for all five targets. Lens-to-target distance variations were within ±150 μm for all five target elements. More details on these measurements can be found in [13]. Later during a search for optimal focusing lens-to-target position, it was found that ion pulse shapes are not affected by lens-to-target distance variations within ±2 mm, so the effect of target "flatness" is negligible for all measurements described below.

III. RESULTS AND DISCUSSION

A. Optimal target-to-focusing lens distance search

At first, we verified the influence of a FC meshed electrode potential on the ion current measurements. No influence was observed for potentials below -100 V, and FC suppressor potential was set to -500 V for all further measurements described below.

Five laser shots were fired onto the same target spot and after the fifth laser shot target was moved either vertically or horizontally by 500 μm to setup new ("fresh") target surface for following five laser shots. The laser was operated in a single shot mode using an external trigger, with average pulse energy of 1.27 mJ and energy standard deviation of 0.06 mJ.

An aluminum target was used to determine the optimal target-to-focusing lens distance. A significant difference was observed for ion pulse shapes between first, second and subsequent shots onto the same target spot, so ion pulse shapes were always compared separately for different number of laser shots onto the same target spot. A 50 Ohm oscilloscope input resistor was used to record ion pulse shapes for different target-to-focusing lens distances. At first, the target-to-lens distance was scanned around the nominal lens focal position (F = 300 mm) in wide range of ± 12 mm with 1 mm step and the corresponding FC signals were recorded for each target position. Positive and negative target shifts from lens focal position correspond to shorter and longer target-to-lens distances correspondently. The results for the third shot onto the same spot of aluminum target for different target-to-focusing lens distances are presented in Fig. 3 (a, b).

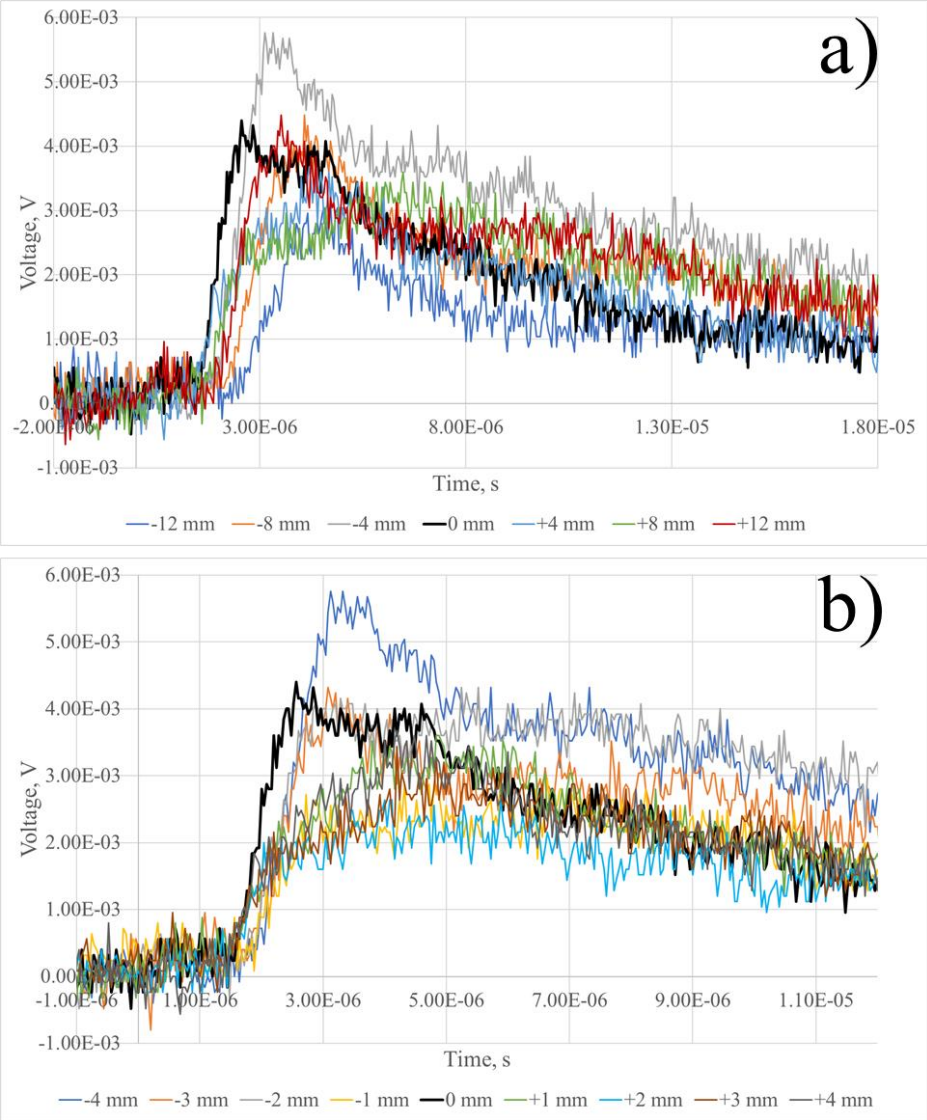

FIG. 3 (a, b). FC signals for different target-to-focusing lens distances (Al target, 3-rd laser shot onto the same target spot, 50 Ω FC load resistor): a – FC signals for target positions from -12 mm to +12 mm with 4 mm target position shift are plotted, b – FC signals for target positions from -4 mm to +4 mm with 1 mm target position shift are plotted, FC signals corresponding to target-to-lens distance equal to nominal lens focal length of 300 mm (z = 0 mm) are highlighted by black thicker lines in both figures.

One can see that target-to-lens distance equal to nominal lens focal length of 300 mm (0 mm shift in Fig. 3 (a, b)) is the optimal for ion generation providing shortest arrival time of fastest ions and one of the highest amplitudes of ion signal. We performed 5 shots onto the same target spot for each target position. The same conclusion was derived for all other laser shot numbers onto the same Al target spot. It was found that distribution of ion pulse shape on target-to-lens distance is quite wide. Target shifts within ± 2 mm do not affect the ion pulse shapes. We also checked if there is any fine structure in the distribution by scanning target position around nominal lens focal length within ± 1 mm range using 100 μm step. No fine structure was found. It confirms that degree of target "flatness" for all 5 targets used (which was within ± 150 μm as mentioned above) does not affect ion yield measurements for whole range of vertical and horizontal target translations. Target-to-lens distance was set to the nominal focal lens distance of 300 mm for all ion yield measurements described below.

B. Target crater shape and size

A Nikon Eclipse LV150 optical microscope was used to record target crater image and to measure crater size after targets were removed from vacuum chamber. Craters were studied for different irradiation conditions for all 5 targets. Microscope software allowed us to approximate every cross section of crater image by ellipse and measure length of both ellipse axis and ellipse area. The examples of crater images and their analysis are presented in Fig. 4 (a, b, c, d) for 5 and $3.7 \cdot 10^3$ laser shots onto the same spot of Ta target with 1.27 mJ laser pulse energy.

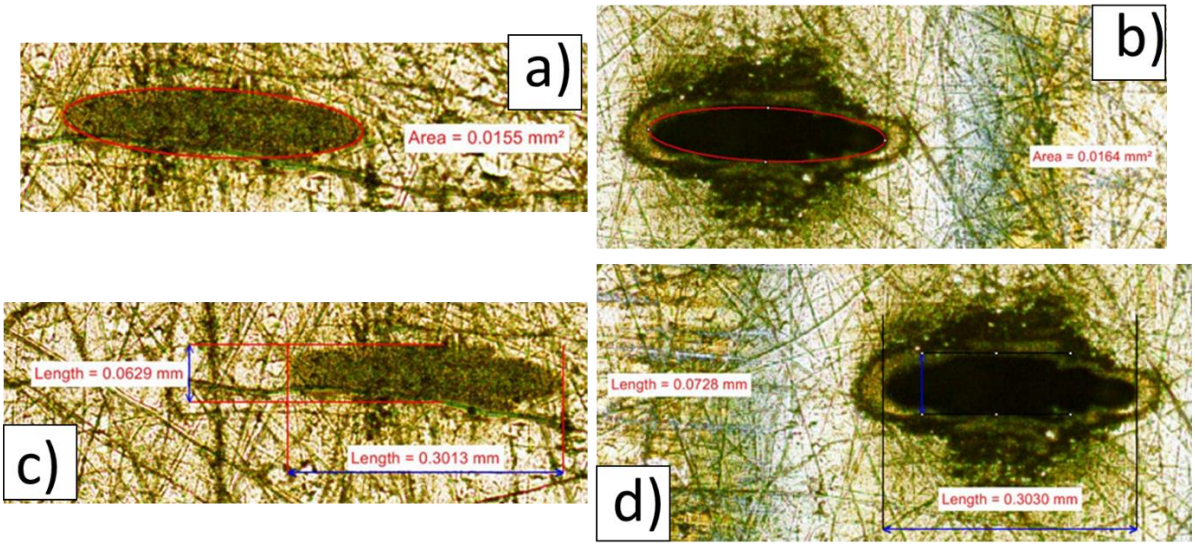

FIG. 4 (a, b, c, d). Crater images approximated by ellipses and their dimensions (length of horizontal and vertical axis, and the area of elliptical approximation of crater cross section) for Ta target with 1.27 mJ laser pulse energy (a and c – 5 laser shots, b and d – $3.7 \cdot 10^3$ laser shots onto the same target spot).

As it was mentioned above, for ultrashort laser pulses with pulse durations less than 10 ps there is no zone affected by heat conductance around laser spot [18]. Crater size in this case should be much closer to laser spot size at the target surface than it is in the case of ns-laser in which the crater is significantly affected by ablation of material surrounding laser spot due to heat conductivity in the target material. However, even in the case of ps-laser for our target irradiation conditions, the crater is larger than laser focal spot at the target surface because laser beam has Gaussian transverse profile and target ablation threshold is significantly lower than the laser intensity at which beam size should be identified. As one can see from Fig. 4 (a, b, c, d) crater cross section has close to elliptical shape with horizontal axis being about 4 times longer than vertical one and with area of about 0.016 mm^2. The reason for such asymmetry will become more clear from microscope crater images created during optimal target-to-lens distance search which are shown in Fig. 5 (a, b, c, d).

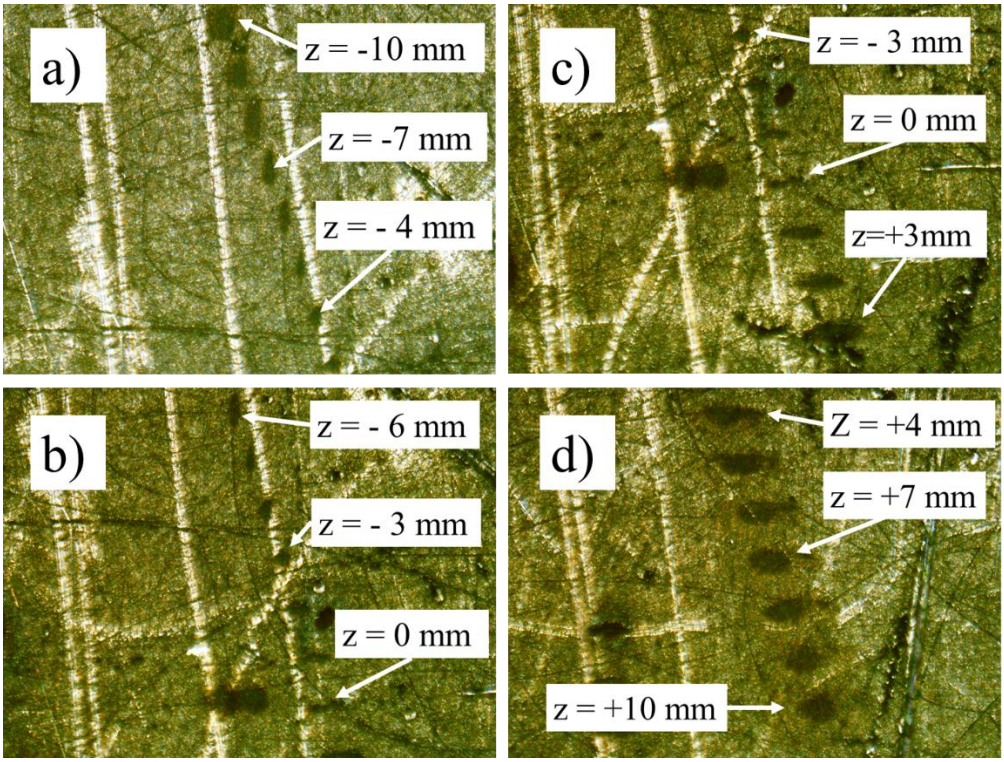

FIG. 5 (a, b, c, d). Images of craters created during optimal target-to-lens distance search (target translations around nominal lens focal distance of 300 mm within ±10 mm range with 1 mm step, 5 laser shots onto the same target spot): a – from -10 mm to – 4 mm, b – from -6 mm to 0 mm, c – from -3 mm to +3 mm, d – from +4 mm to +10 mm. All negative and positive z values correspond to target positions behind and in front of nominal focal position, respectively. z = 0 mm corresponds to target-to-lens distance equal to nominal lens focal length of 300 mm.

One can see that crater cross sections have elliptical shapes with vertical axis longer than horizontal one for all target positions with z < -3 mm (behind the nominal focal target position) being converted to elliptical shapes with horizontal axis longer than vertical one for all target positions with z > -3 mm (target moving closer to focusing lens). Crater cross section has close to round shape for target position with z = -3 mm. Such crater asymmetry is most likely caused by astigmatism of focusing lens as we have used ordinary lens without correction of any aberrations. One should note that the best ion yield (highest ion current amplitude, fastest ion arrival to FC) was found for elliptical laser spot at target position with z = 0 mm (nominal lens focal length of

300 mm) and not for the most symmetric laser spot at target position with z = -3 mm (3 mm behind the nominal focal position).

Aluminum crater dimensions for different target irradiation conditions (target positions, number of laser shots onto the same target spot, laser pulse energy and rep-rate) are summarized in Table I.

Table I. Aluminum crater dimensions for different target irradiation conditions – number of laser shots onto the same target spot, target-to-focusing lens distance, laser pulse energy and rep-rate (S – area of crater cross section, A and B – vertical and horizontal axis of elliptical approximation of crater cross section, LE1.0 – maximal laser pulse energy of 1.27 mJ, LE0.2 – laser pulse energy attenuated to 20% of maximal energy (0.254 mJ)).

Irradiation parameters	Z=-3mm close to round 5 shots	Z=-6mm behind focus 5 shots	Z=0mm ion yield focus 5 shots	Z=0mm LE1.0 25 Hz $1.1\cdot10^3$ shots	Z=0mm LE0.2 25 Hz $2.7\cdot10^3$ shots	Z=0mm LE1.0 400 Hz $2.2\cdot10^4$ shots
S, mm^2	0.019	0.009	0.014	0.021	0.017	0.017
A, mm	0.15	0.27	0.06	0.08	0.08	0.07
B, mm	0.16	0.04	0.31	0.32	0.29	0.29

One can see that area of crater cross sections is in the range of 0.009 – 0.021 mm^2 while length of ellipse axis varies from 40 µm to 320 µm depending on target-to-focusing lens distance and target irradiation conditions. Craters for 5 laser shots are smaller than craters for thousands of shots onto the same target spot as one would expect. Areas of crater cross sections for all other target elements are similar to the Al target cross section areas in the case of both 5 shots and 10^3 – 10^4 shots onto the same target spot as illustrated by Fig. 6 (a, b). Different target irradiation conditions – laser pulse energy, laser rep-rate and number of laser shots onto the same target spot are specified in the Fig. 6 (a, b) caption for each crater area measurement.

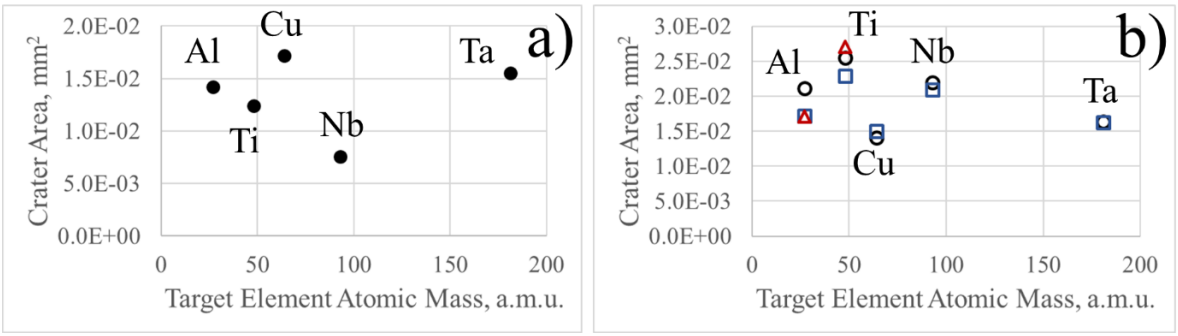

FIG. 6 (a, b). Area of craters for different target elements (Al, Ti, Cu, Nb and Ta) and different target irradiation conditions (a – 1.27 mJ laser pulse energy and 5 laser shots onto the same target spot, b – thousands of laser shots onto the same target spot: Al target – circle – 1.27 mJ, 25 Hz laser rep-rate, $1.1 \cdot 10^3$ shots; square - 0.25 mJ, 25 Hz laser rep-rate, $2.7 \cdot 10^3$ shots; triangular - 1.27 mJ, 400 Hz laser rep-rate, $2.2 \cdot 10^4$ shots; Ti target – 1.27mJ, 25 Hz: circle – $1.0 \cdot 10^3$ shots, square – $2.1 \cdot 10^3$ shots, triangular – $3.1 \cdot 10^3$ shots; Cu target - 1.27mJ, 25 Hz: circle – $3.0 \cdot 10^3$ shots, square – $1.6 \cdot 10^3$ shots; Nb target - 1.27mJ, 25 Hz: circle – $2.9 \cdot 10^3$ shots, square – $4.5 \cdot 10^3$ shots; Ta target - 1.27mJ, 25 Hz: circle – $3.7 \cdot 10^3$ shots, square – $1.8 \cdot 10^3$ shots).

Most of crater cross section areas are in the range of 0.01 – 0.017 mm^2 and 0.015 – 0.025 mm^2 for 5 laser shots and 10^3 – 10^4 laser shots onto the same target spot respectively, for all target elements.

The dependence of crater cross section area on laser pulse energy was studied for Ta target and the result obtained is shown in Fig. 7.

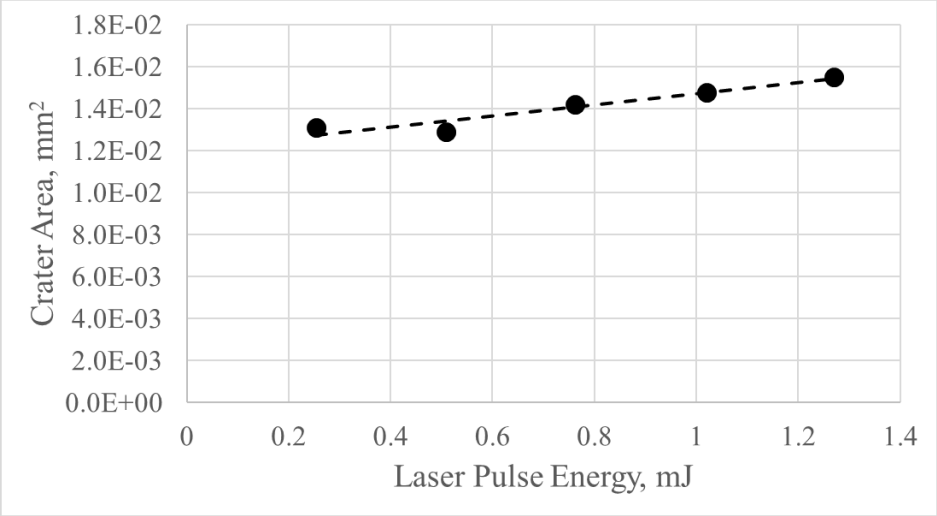

FIG. 7. Dependence of crater cross section area on laser pulse energy for Ta target (5 laser shots onto the same target spot).

All craters were created by 5 laser shots onto the same target spot. As one would expect, crater cross section areas are smaller for lower laser pulse energy. Dependence of crater cross section area on laser pulse energy is linear with minor line slope.

Let us estimate the laser power density at the target surface. If it is limited by diffraction, the focal spot diameter (d_f) of a Gaussian beam with wavelength λ=1064 nm, and the corresponding laser power density (P) within the focal spot are defined by following equations:

$$d_f = \frac{4}{\pi} \cdot \lambda \cdot \frac{F}{D} \qquad (1)$$

$$P = \frac{4 \cdot E}{\tau \cdot \pi \cdot d_f^2} \qquad (2)$$

where F is focusing lens focal distance

D is laser beam diameter

E and τ are laser pulse energy and laser pulse duration.

In our case F = 300 mm, D ≈ 10 mm, E ≈ 1.27 mJ and τ ≈ 8 ps. The diffraction limited focal spot size is about 41 μm and laser power density at the target surface is about $1.2 \cdot 10^{13}$ W/cm^2. As one can see from the above discussion, focal spot size and laser power density at the target surface were significantly affected by astigmatism of the focusing lens. The exact power density reduction

factor cannot be extracted from crater size measurements as was mentioned above. Nevertheless, such reduction factor certainly cannot be neglected and should be considered.

C. Dependence of ion yield on shot number onto same target spot

In early experiments, we used a 50 Ω FC load resistor because it allowed us to record the true time dependencies of ion current. However, the signal-to-noise ratio was relatively low even in the case of Al target (see Fig. 3 (a, b)) for which ion current is the highest among all 5 targets we used. To resolve high noise issue especially for heavier target elements with lowest ion currents we used a 1 kΩ FC load resistor for all further measurements of ion current time dependencies. That gave us a factor of 20 enhancement of recorded FC voltage and significant improvement of signal-to-noise ratio. At the same time, it would be beneficial not to lose the correct information on time dependencies of the measured ion currents. To check that, we have compared ion signals for Al target (which provide fastest ion signals among all 5 targets used) recorded with 50 Ω (Fig. 8 (a)) and 1 k Ω (Fig. 8 (b) FC load resistors, respectively. All signals were averaged over 3 laser shots for the same target irradiation conditions.

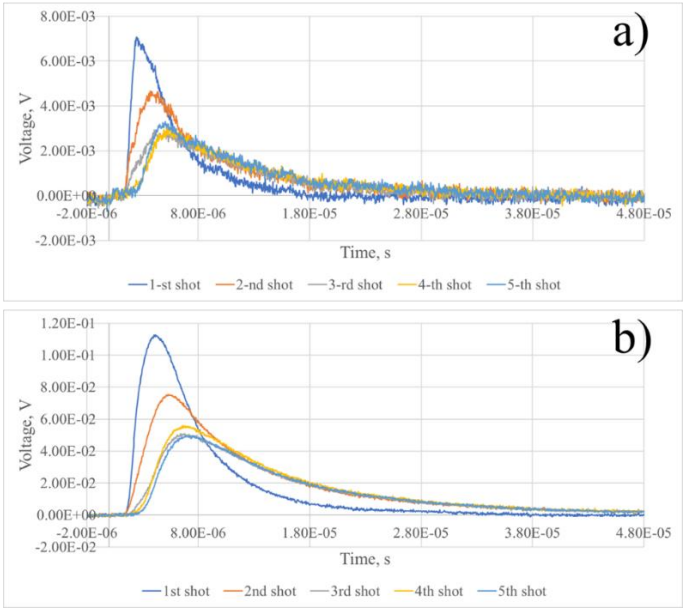

FIG. 8 (a, b). FC signals measured with 50 Ω (a) and 1 kΩ (b) FC load resistors for Al target and for the first five laser shots onto the same target spot (each curve is averaged over 3 laser shots).

Detailed comparison of FC signals for Al target recorded at 50 Ω and 1 kΩ FC load resistors reveals that ion current time dependence is reproduced with accuracy of about 30% for the first shot at Al target (fastest ion signal) and of about 10% for any short number equal or above 3 onto the same target spot. The accuracy for heavier elements is better than 10% because FC signals are slower for heavier elements as illustrated by Fig. 9 where FC signals for 3-rd shot onto the same target spot are presented for all five target elements used.

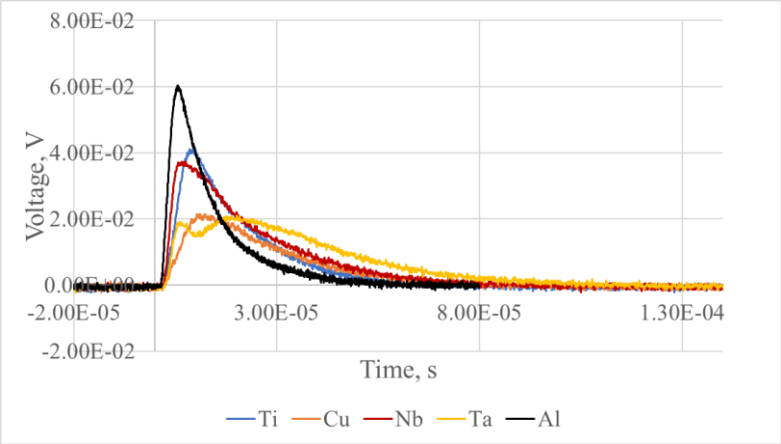

FIG. 9. FC signals for the 3rd laser shot for all five target elements measured using a 1 kΩ resistor (each curve is averaged over 3 laser shots).

Taking this fact into account, one can still extract relatively accurate information on ion time and energy, using the time dependencies of ion current recorded with a 1 kΩ FC load resistor for all five target elements.

As one can see from Fig. 8 (a, b), time dependencies of Al ion current for the first and the second laser shots onto the same target spot are quite different from ion current time dependencies for subsequent shots. Ion current amplitudes are the highest for the first shot, about 30% lower for the second shot and about 60% lower for subsequent shots. Ions are the fastest for the first shot, slightly slower for the second shot and significantly slower for subsequent shots. Further studies revealed that ion current pulse shape does not further change for at least about 100 subsequent laser shots onto the same target spot after the third shot. Similar behavior was observed for all other target elements as shown in Fig. 10 (a, b, c, d). There were two exceptions: ion yield for only

the first laser shot was different from subsequent shots for the Ti target (Fig. 10 (a)), and the second laser shot provided the highest amplitude of ion current for the Nb target (Fig. 10 (c).

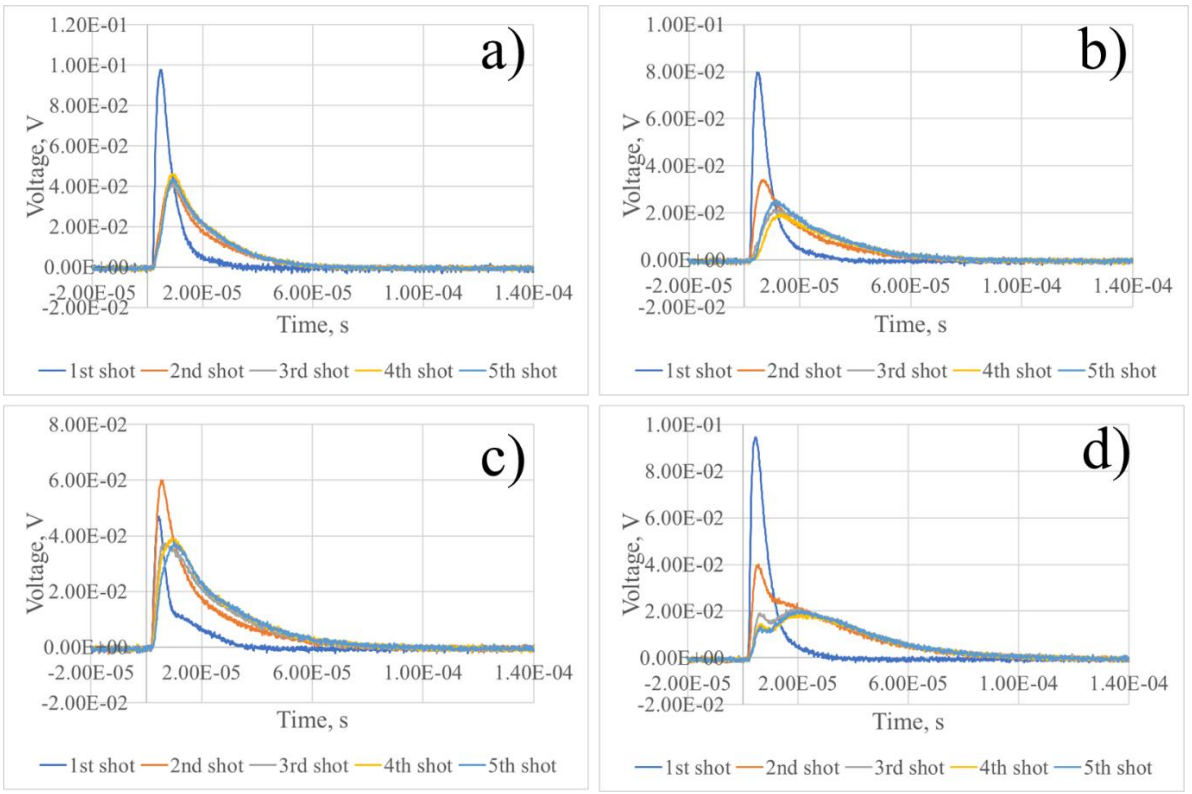

FIG. 10 (a, b, c, d). FC signals for Ti (a), Cu (b), Nb (c) and Ta (d) targets and for first five laser shots onto the same target spot (each curve is averaged over 3 laser shots).

One of the possible explanations for such significant differences in time dependencies of ion current for first, second and subsequent shots onto the same target spot could be formation of target crater and its influence on laser plasma generation, but then there is an open question - why is there no difference in ion time dynamics for the third and subsequent shots as any further shot still contribute to crater modification. So, it is quite unlikely that crater formation plays significant role in the effect observed. Another possible explanation for this effect can be presence of some amount of impurities at the new (“fresh”) target surface before first laser shot hit it. That can explain why ion yield for the first laser shot is different from subsequent shots onto the same spot. However, one can expect that all impurities will be removed from the target surface within the laser focal

spot after the first laser shot and the ion yield for the second and the third shots would already be identical which was not observed for the various target elements except Ti. Some contributions to this phenomenon can be explained by initial surface roughness and by possible modification of material physical properties caused by laser radiation itself. Further investigations are required to better understand this effect.

Total charge carried by ions registered by the FC for each laser shot was measured using the 1 MΩ oscilloscope input impedance as the FC load resistor. The typical FC signal recorded by oscilloscope in this case is presented in Fig. 11 (a, b).

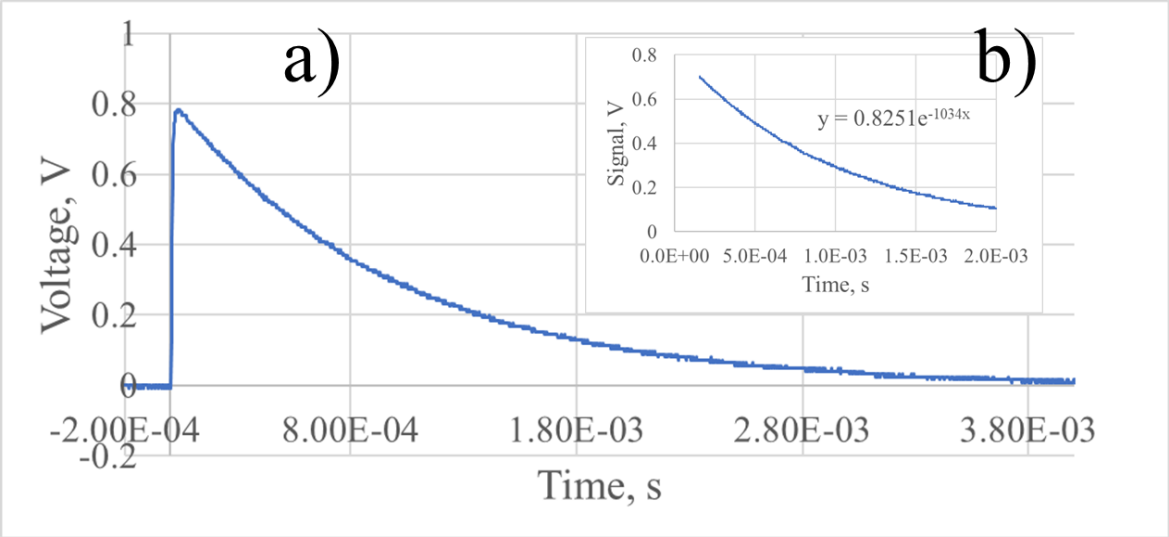

FIG. 11 (a, b). FC signal measured at 1 MΩ FC load resistor (a) and exponential approximation of its voltage time decay (b) (Al target, first laser shot).

The ion current was integrated by the measuring system capacitance which consists of the sum of FC itself, signal cable and oscilloscope input capacitances. Total capacitance was measured using a multimeter and was displayed as 1.003 nF. The total capacitance calculated from the exponential voltage time decay (Fig. 11 (b)) was found to be equal to 0.967 nF, in agreement with the value measured by multimeter. For all further calculations of total charge of registered ions integration circuit capacitance of 1 nF was used. The exponential voltage time decay constant (1.034 ms (Fig. 11 (b))) is much longer than ion pulse durations for all target elements (less than

100 μs (Fig. 10 (a, b, c, d))), so the total charge of registered ions was calculated using following equation:

$$N_i = A \cdot C \qquad (3)$$

A is registered voltage amplitude in Volts

C is integration circuit capacitance in Farads.

Dependencies of total charge carried by ions registered by the FC on laser shot number onto the same target spot for all five target elements are presented in Fig. 12 (a, b, c, d, e). All data points were averaged over three laser shots for the same measurement conditions.

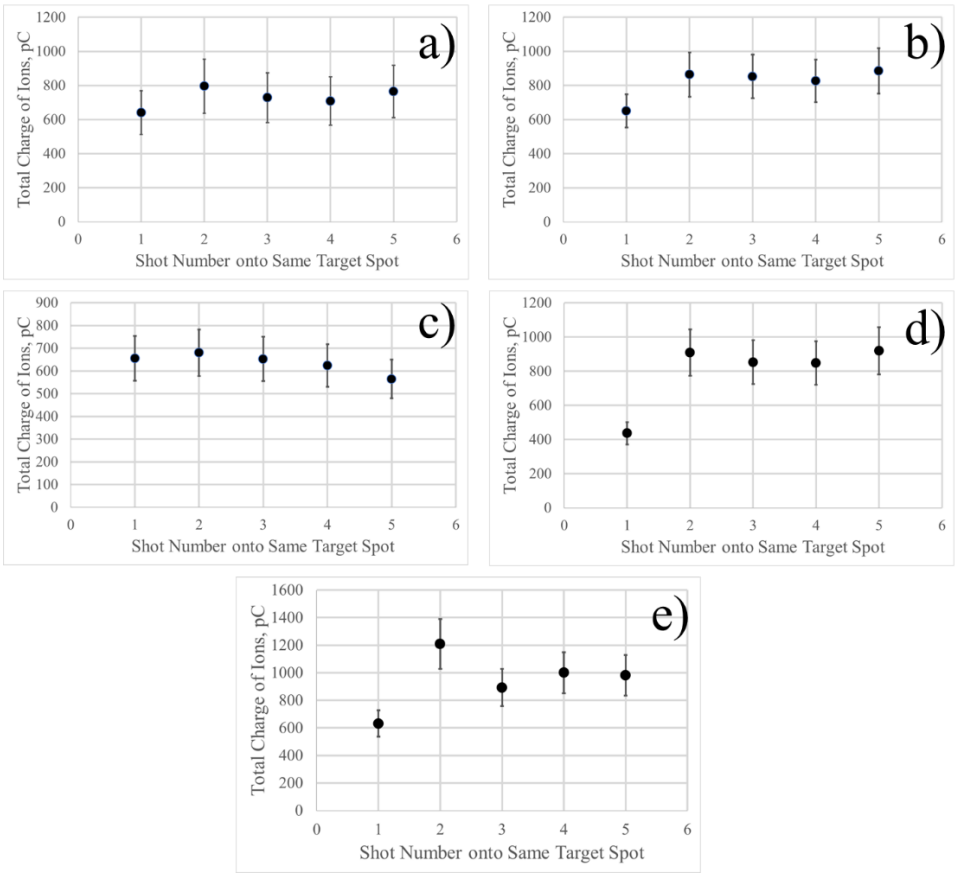

FIG. 12 (a, b, c, d, e). Dependencies of total charge of ions registered by the FC on laser shot number onto the same target spot for all five target elements (a – Al target, b – Ti target, c – Cu target, d – Nb target and e – Ta target).

One can see that the total charge of ions registered by the FC is independent of the number of laser shots onto the same target spot for all target elements, except the heaviest elements of Nb and Ta, for which first laser shot provides lower ion yield (see Fig. 13 as well).

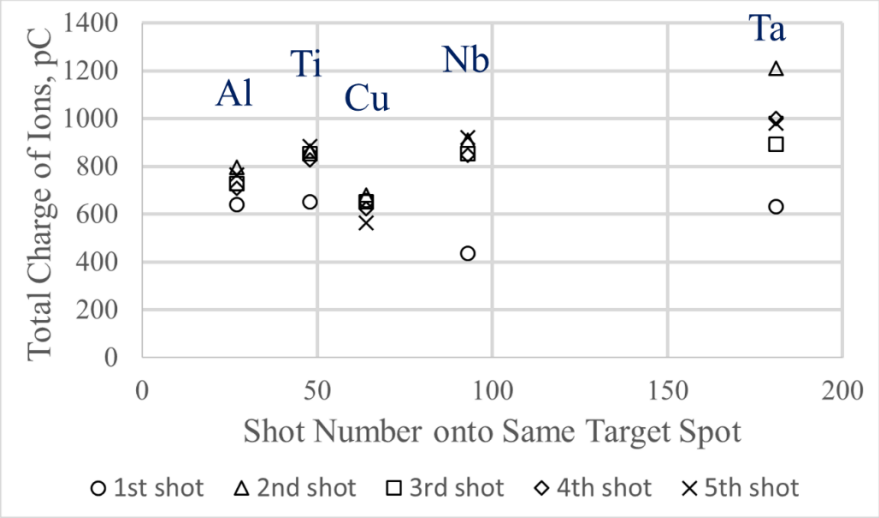

FIG. 13. Total charge of ions registered by the FC for all target elements used and for different laser shot number onto the same target spot.

The total charge of ions is almost independent on target element and in most cases, it is in the range of 600 – 1000 pC per laser shot. Measured ion current amplitudes and pulse durations (FWHM) together with estimated total number of ions registered by the FC are summarized in Table II.

Table II. Measured ion current amplitudes (I) and pulse durations (FWHM) (Δt) together with estimated total number of ions registered by FC (N) (5-th laser shot onto the same target spot averaged over 3 laser shots for all target elements).

Element	Al	Ti	Cu	Nb	Ta
I, μA	48	43	25	37	20
Δt, μs	11.5	15.5	20.4	20.2	42.1
N	$4.8 \cdot 10^9$	$5.5 \cdot 10^9$	$3.5 \cdot 10^9$	$5.8 \cdot 10^9$	$6.1 \cdot 10^9$

For the estimation of the number of ions, we assumed that most of the ions are singly charged because the laser power density at the target surface is relatively low. Some small fraction of registered ions can be in higher charge states and could affect the accuracy of such estimation.

D. Dependence of ion yield on laser pulse energy

The influence of the laser pulse energy on ion yield was studied for the lightest (Al) and the heaviest (Ta) target elements. The laser pulse energy was varied using internal laser attenuation control knob to provide 5 discrete values of 20%, 40%, 60%, 80% and 100% of maximum laser energy of 1.27 mJ per pulse. Laser pulse duration and laser beam divergence should not be affected by energy attenuation settings according to laser manufacturer; therefore, the laser power density at the target surface should be proportional to the laser pulse energy. Dependencies of the total charge of ions registered by the FC for different shot number onto the same laser spot on laser pulse energy for Al and Ta targets are presented in Fig. 14 (a, b).

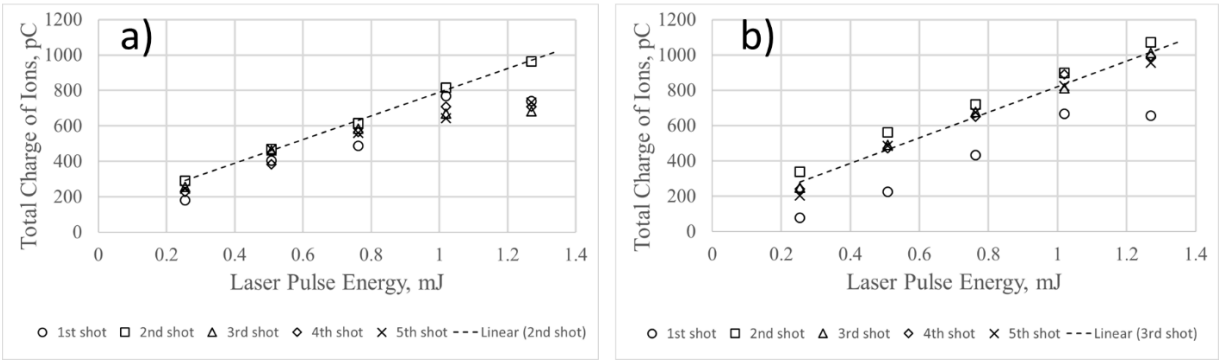

FIG. 14 (a, b). Dependencies of the total charge of ions registered by the FC for different shot number onto the same target spot on laser pulse energy for Al (a) and Ta (b) targets elements.

One can see that the total charge of registered ions is linearly proportional to laser pulse energy for all shot numbers onto the same target spot and for both target elements. Ion yield is almost independent on shot number onto the same target spot for Al target in the whole range of studied laser pulse energies. The first laser shot provides lower ion yield than subsequent shots onto the same target spot for Ta target in the whole range of studied laser pulse energies. Also, there is a tendency for ion yield saturation for the highest laser pulse energy of 1.27 mJ for both target elements.

FC signals for different laser pulse energies and different laser shot number onto the same target spot are presented in Fig. 15 (a, b, c, d, e, f) for Al and Ta targets.

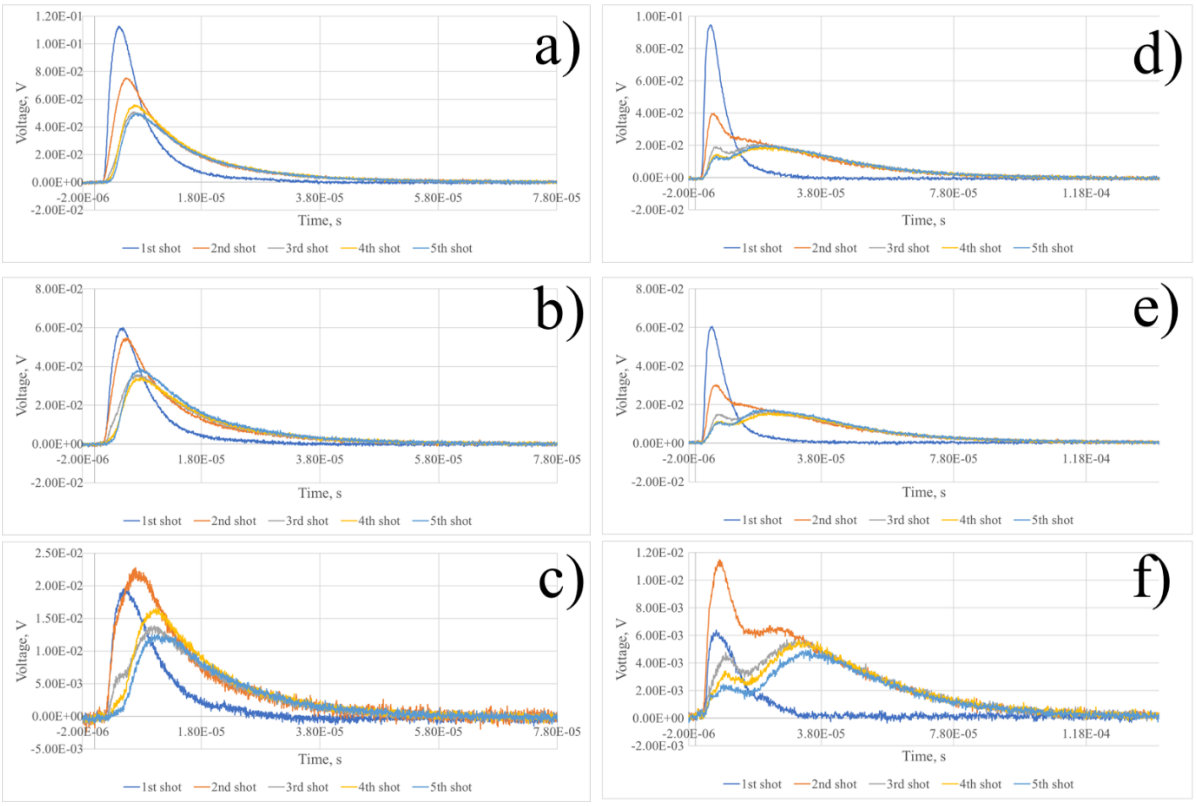

FIG. 15 (a, b, c, d, e, f). FC signals for different laser pulse energies and different laser shot number onto the same target spot for Al and Ta targets (Al target: a – 1.27 mJ, b – 0.762 mJ, c – 0.254 mJ; Ta target: d – 1.27 mJ, e – 0.762 mJ, f – 0.254 mJ).

One can see that the ion current amplitudes are the highest for the first shot, lower for the second shot and even lower for subsequent shots for the highest laser pulse energy of 1.27 mJ for both Al and Ta targets as was already mentioned earlier. These amplitudes are closer to each other (almost equal for Al target) for the first and the second shots for intermediate laser pulse energy of 0.762 mJ. The ion current amplitudes become higher for Al target and even higher for Ta target for the second shot compared to the first shot for the lowest laser pulse energy of 0.254 mJ.

FC signals for different laser pulse energies depending on shot number onto the same target spot for Al and Ta targets are presented in Fig. 16 (a, b, c, d, e, f, g, h).

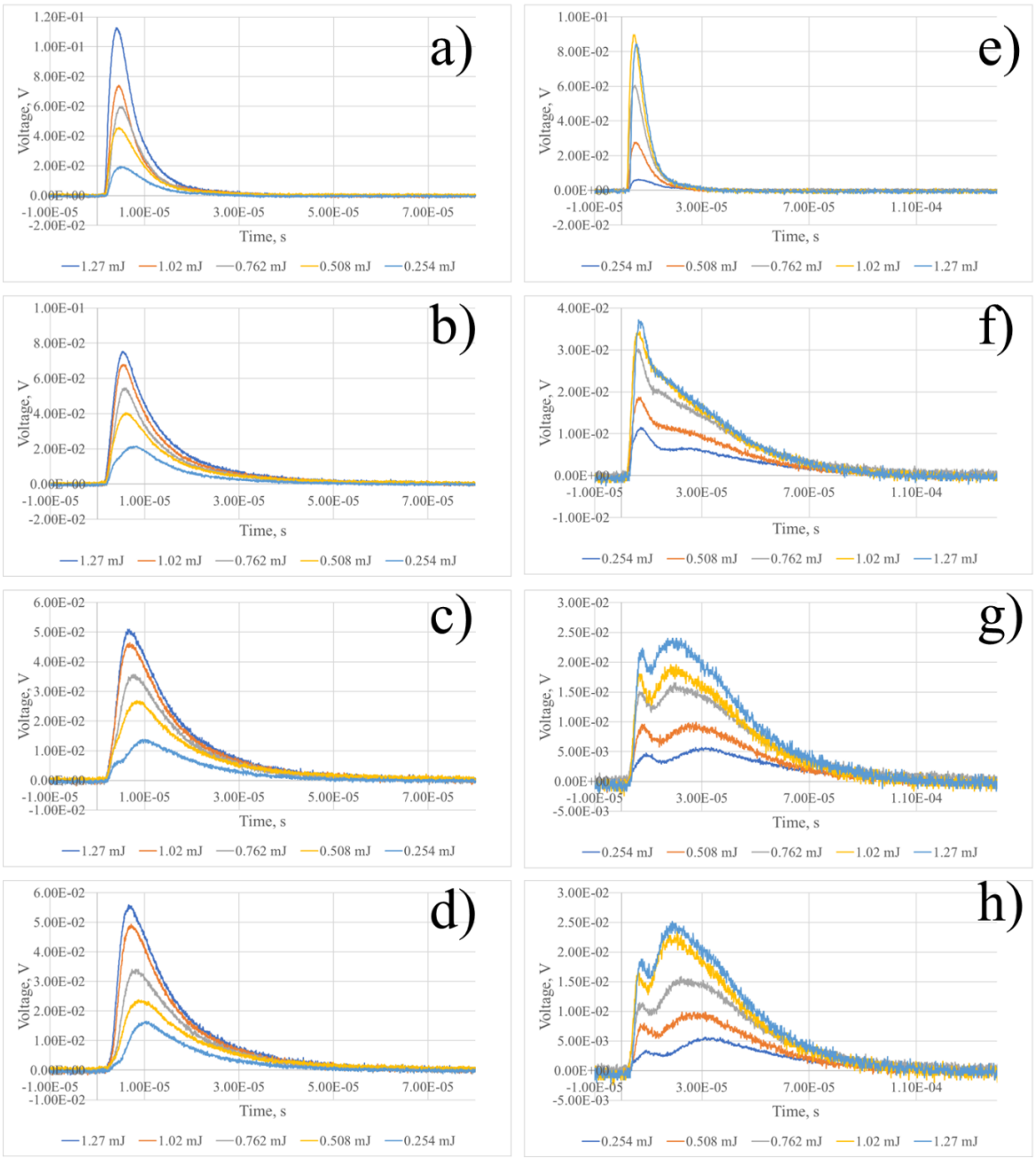

FIG. 16 (a, b, c, d, e, f, g, h). FC signals for different laser pulse energies depending on shot number onto the same target spot for Al and Ta targets (Al target: a – first shot, b – second shot, c – third shot, d – forth shot; Ta target: e – first shot, f – second shot, g – third shot, h – forth shot).

One can see that ion current is consistently decreasing with decreasing laser pulse energy for both Al and Ta target elements. The time, corresponding to ion current peak amplitude, become

longer for lower laser pulse energy for the second and subsequent laser shots onto the same target spot, as expected. Surprisingly, this time for the first shot doesn't depend on laser pulse energy for either target element. Ion current pulses for Ta target have a well-defined two peak time structure for the third and the fourth shots onto the same spot. There is a very weak dependence of the first peak arrival time on the laser pulse energy and much stronger dependence of the second peak arrival time on that parameter for Ta target.

E. Ion energy distributions

Time dependencies of ion current measured by the FC can be transformed into ion charge energy distributions using following equations:

$$\frac{dQ}{dE} = \frac{dQ}{dt} \cdot \frac{dt}{dE} = I(t) \cdot \left(\frac{dE}{dt}\right)^{-1} = I(t) \cdot \frac{t^3}{M \cdot L^2} \qquad (4)$$

$$E(t) = \frac{1}{2} M V^2 = \frac{1}{2} M \frac{L^2}{t^2} \qquad (5)$$

where I is ion current

t is time

E and M are ion energy and mass

Q is charge carried by ion flux

L is FC to target distance.

After initial application of this transformation to experimental data it was realized that any noise in the time dependence of ion current will be greatly enhanced in the ion charge energy distribution, especially in the region of low energies (long times). A noise suppression algorithm was applied to all time dependencies of ion current prior to their transformation to ion energy distributions to minimize such enhancement. All time dependencies of ion current were averaged over 10 adjacent points and average current value were assigned to the middle point within averaging time interval for the entire FC signal recorded by the digital oscilloscope. As a result, noise at ion energy distributions was significantly suppressed. In addition, high energy tails of ion energy distributions were limited at the level of 10% from maximum ion current. Less than 1% of all ions were eliminated from the distributions in this way. At the same time, it allows to avoid artificial high energy tails caused by residual noise of ion current at shortest arrival times to FC.

Ion energy distributions for all 5 target elements are presented in Fig. 17 (a, b, c, d, e) for the first 5 laser shots onto the same target spot.

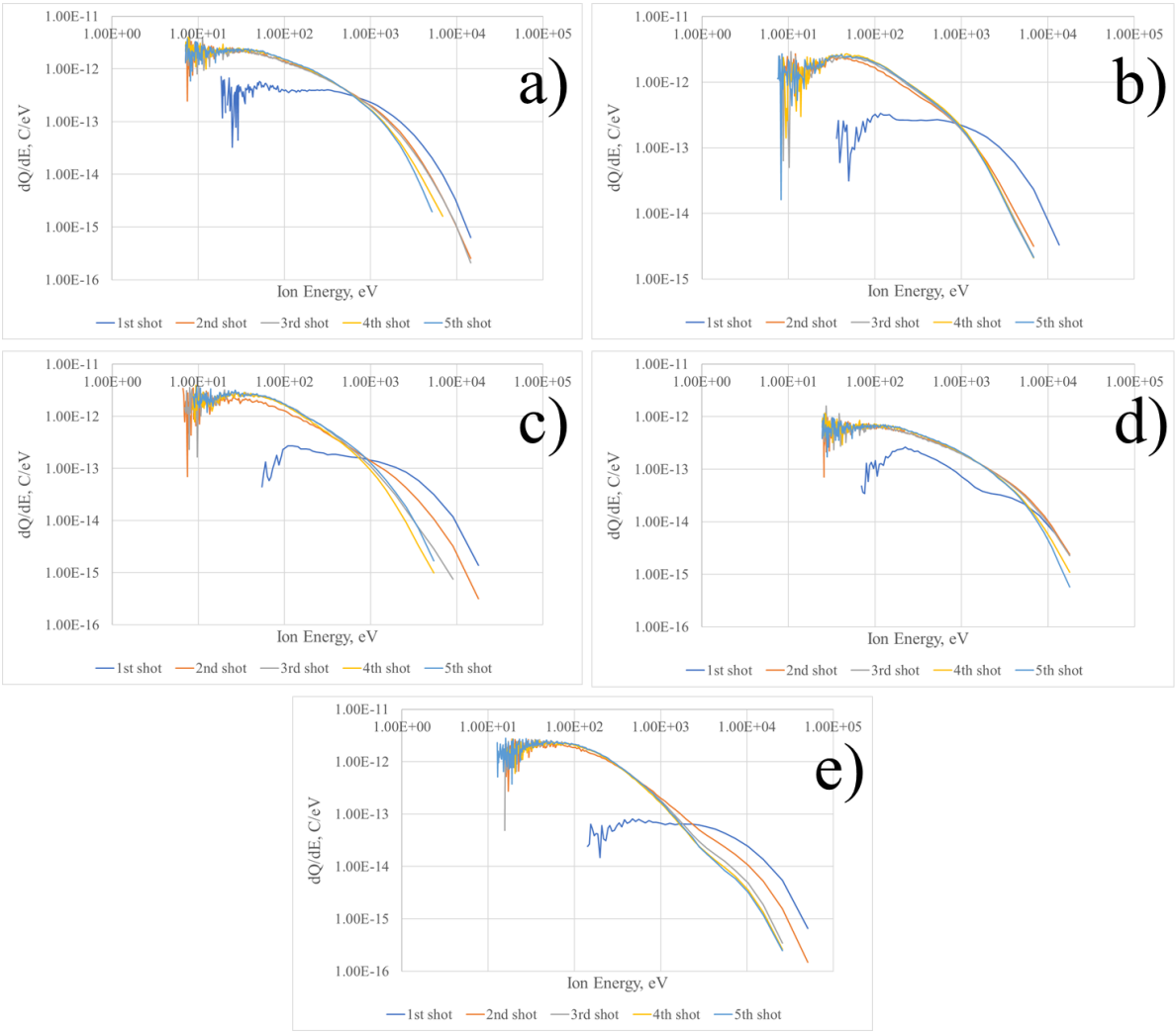

FIG. 17 (a, b, c, d, e). Ion energy distributions for all 5 target elements for the first 5 laser shots onto the same target spot (laser pulse energy 1.27 mJ: a – Al target, b – Ti target, c – Cu target, d – Nb target, e – Ta target).

One can see that ion energy distributions for all target elements have a plateau or a slight peak in the energy range of 10 - 100 eV and long low-intensity energy tail up to tens of keV. For the first laser shot, low energy part of distribution is significantly suppressed, but high energy tail is

well enhanced for all target elements. The high energy tail is enhanced for the second laser shot as well, being almost identical to subsequent laser shots onto the same target spot in lower energy range for all target elements.

Ion energy distributions for all target elements for the second and fourth shots onto the same target spot are shown in Fig. 18 (a, b).

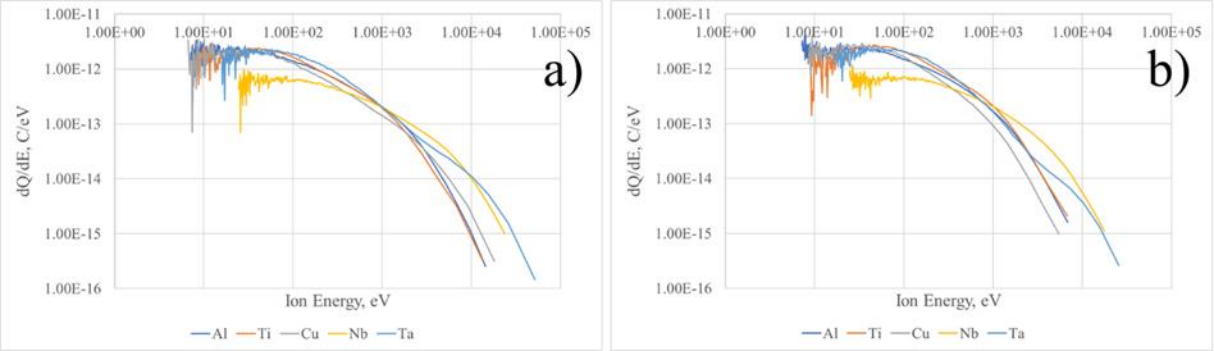

FIG. 18 (a, b). Ion energy distributions for all target elements for the second (a) and fourth (b) shots onto the same target spot.

One can see that ion energy distributions for lighter target elements (Al, Ti and Cu) are very similar for both the second and fourth shots onto the same target spot, while there is a more intense high energy tail for heavier target elements (Nb and Ta). Nb distributions have lower intensity in the low energy segment as well.

Al and Ta ion energy distributions for first 5 laser shots onto the same target spot are presented in Fig. 19 (a, b, c, d, e, f) for different laser pulse energies.

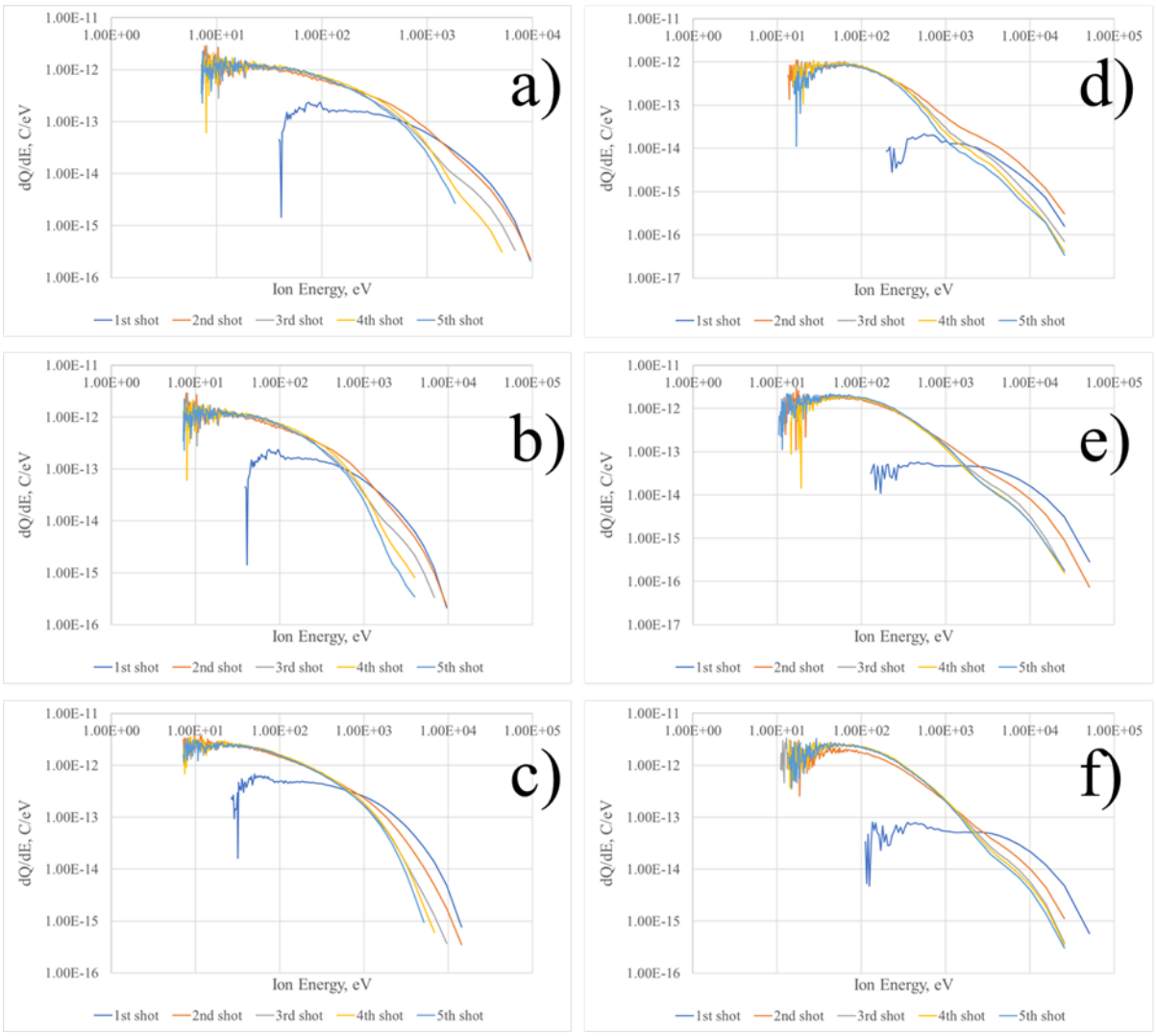

FIG. 19 (a, b, c, d, e, f). Al and Ta ion energy distributions for the first 5 laser shots onto the same target spot for different laser pulse energies (Al target: a – 0.254 mJ, b – 0.762 mJ, c – 1.27 mJ; Ta target: d – 0.254 mJ, e – 0.762 mJ, f – 1.27 mJ).

Ion energy distributions have very similar properties for the whole range of laser pulse energies for both Al and Ta target elements as was described earlier in relation to Fig. 17 (a, b, c, d, e). The only difference to be mentioned here is that for laser pulse energy of 0.254 mJ, the second shot onto the same target surface provide almost equal (Al) and even higher (Ta) tail in the range of ion energies above 500 eV compared to the first shot onto the same target spot. For laser pulse energy of 1.27 mJ such a comparison shows the opposite result.

Al and Ta ion energy distributions for the first, the second and the fourth shots onto the same target spot for different laser pulse energies are presented in Fig. 20 (a, b, c, d, e, f).

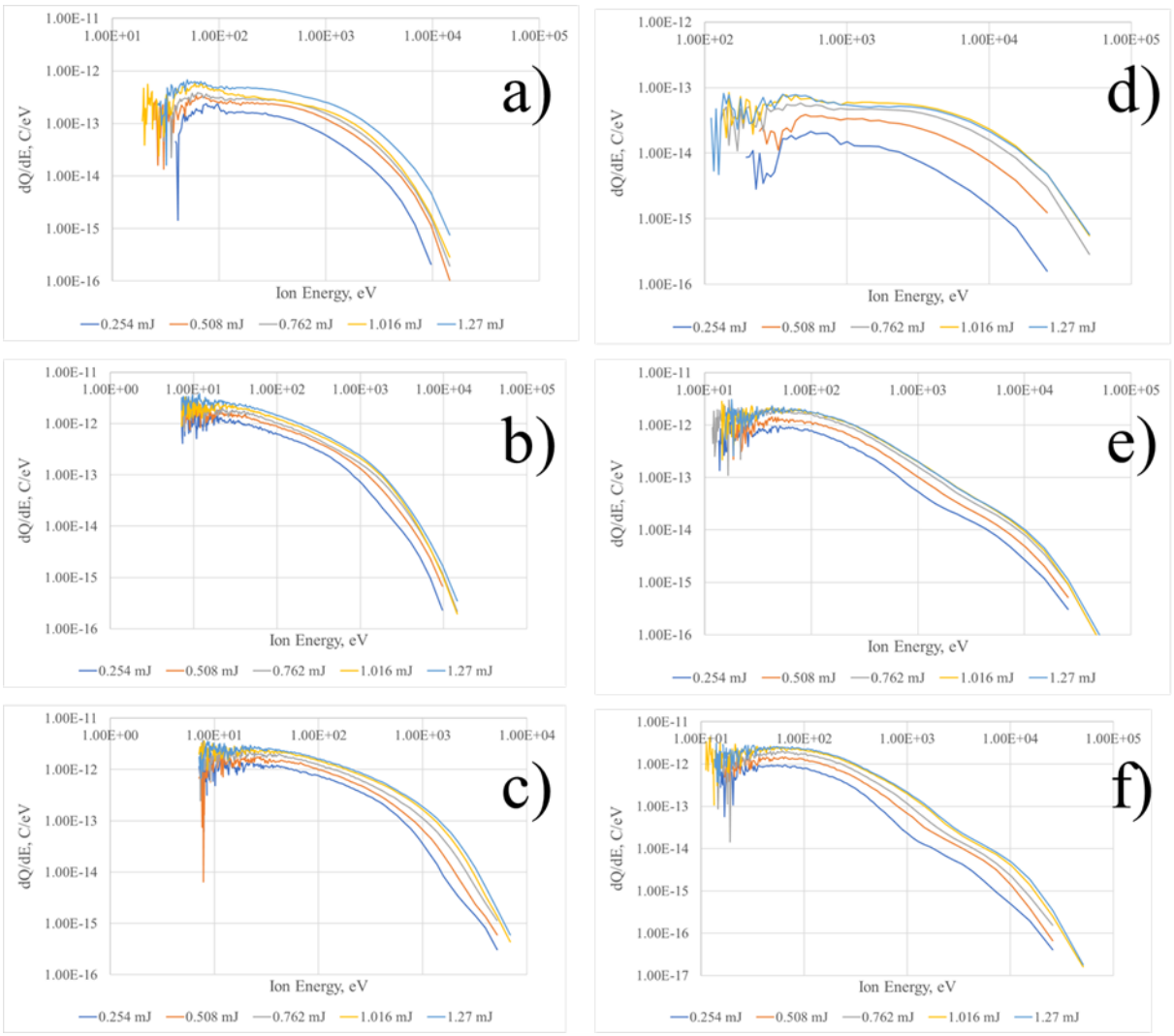

FIG. 20 (a, b, c, d, e, f). Al and Ta ion energy distributions for the first, the second and the fourth shots onto the same target spot for different laser pulse energies (Al: a – first shot, b – second shot, c – fourth shot; Ta: d – first shot, e – second shot, f – fourth shot).

Al and Ta ion energy distributions are decreasing with decreased laser pulse energy without significant re-distribution of ions along the energy scale for all 5 laser shots onto the same target spot. Ta ion energy distributions are more affected by laser pulse energy than Al ion energy distributions.

Summary

Ion generation by a ps-laser with pulse duration of 8 ps and power density at the target surface in the range of 10^{11} – 10^{13} W/cm^2 has been studied for 5 target elements – Al, Ti, Cu, Nb and Ta. Dependencies of ion current, total ion charge and ion charge energy distribution on laser shot number onto the same target spot and laser pulse energy were measured using a Faraday cup. Implementation of a precise 3D target translator allowed us to define the optimal focusing lens – target distance, using the criteria of fastest and highest ion output. It also allowed us to study the dependencies of ion yield on laser shot number onto the same target spot with high reproducibility and in great details for all 5 target elements. Target crater sizes and areas have been characterized using digital optical microscope. Significant distortion of laser focal spot shape and size by astigmatic aberrations of the focusing lens has been identified. Linear dependence of the crater cross section square on the laser pulse energy has been measured for the Ta target.

It was found that time dependencies of ion current for the first and the second laser shots onto the same target spot are quite different from ion current time dependencies for subsequent shots for all 5 target elements. Ion current amplitudes are typically the highest for the first shot, somewhat lower for the second shot and much lower for subsequent shots. In addition, ions are the fastest for the first shot, slightly slower for the second shot and significantly slower for subsequent shots. It is interesting that ion current amplitudes become higher for the second shot compared to the first shot onto the same target spot in the case of lowest laser pulse energy of 0.254 mJ used for measurements. Observed differences are difficult to explain only by either crater formation or by the presence of impurities at the target surface. Initial surface roughness and possible modification of material physical properties by laser radiation itself could contribute to such phenomena as well. Further investigations are required to better understand this effect. Total ion charge registered by the FC is almost independent of target element and on laser shot number onto the same target spot for all target elements. Total charge of registered ions is linearly proportional to the laser pulse energy for all shot numbers onto the same target spot with saturation tendency for the highest laser pulse energy of 1.27 mJ.

Ion energy distributions for all target elements have a plateau or a slight peak in the energy range of 10 - 100 eV and a long low-intensity energy tail up to tens of keV. For the first laser shot,

the low energy part of distribution is significantly suppressed, but the high energy tail is well enhanced for all target elements. Al and Ta ion energy distributions are dropping down with decreasing of laser pulse energy without significant re-distribution of ions along the energy scale for all 5 laser shots onto the same target spot.

Acknowledgment

This work was supported by the US Department of Energy under contract number DE-SC0012704 and by the National Aeronautics and Space Administration.

The authors are grateful to J. Ritter, R. Schoepfer and S. Picataggio for excellent technical support.

References:

[1] S Amoruso, R Bruzzese, N Spinelli and R Velotta, J. Phys. B: At. Mol. Opt. Phys. **32** (1999) R131–R172.

[2] S. Eliezer, *The Interaction of High-Power Lasers with Plasmas*, 1st ed. (IOP Publishing Ltd, London, 2002).

[3] I.V. Roudskoy, Laser and Particle Beams, **14**, 369 (1996).

[4] M.M.Basko and I.P.Tsygvintsev, Computer Physics Communications, **214** , 59 (2017).

[5] Y. A. Byckovsky, V. F. Eliseev, Y. P. Kozyrev, S. M. Silnov, *Laser generator of multi-charged ions for accelerators*, Sov. Patent 324 938, Oct. 1969.

[6] B. Yu. Sharkov, S. Kondrashev, I. Roudskoy, S. Savin, A. Shumshurov, H. Haseroth, H. Kugler, K. Langbein, N. Lisi, H. Magnusson, R. Scrivens, S. Khomenko, K. Makarov, V. Roerich, A. Stepanov, Yu. Satov, Review of Scientific Instruments, 69 (2), pp. 1035-1039 (1998).

[7] T. Tomie, Journal of Micro/ Nanolithography, MEMS, and MOEMS 11(2):021109-1 (2012).

[8] F. Anabitarte, A. Cobo, and J.M. Lopez-Higuera, ISRN Spectroscopy, 285240 (2012)

[9] R. Eason, *Pulsed Laser Deposition of Thin Films: Applications-Led Growth of Functional Materials* (John Wiley & Sons, Inc., 2007)

[10] S. Mishra and V. Yadava, Optics and Lasers in Engineering, 73, pp. 89-122 (2015)

[11] I. Ahmad and W. Akram, *Introductory Chapter: Introduction to Ion Implantation, Ion Implantation - Research and Application*, IntechOpen (2017), https://www.intechopen.com/books/ion-implantation-research-and-application/introductory-chapter-introduction-to-ion-implantation

[12] S. Ikeda, M. Okamura, T. Kanesue, D. Raparia, A. Hershcovitch, K. Yip, K. Takahashi, D. Wu, A. Cannavò and G. Ceccio, Rev. Sci. Instrum. 91, 023304 (2020)

[13] S. Kondrashev, E. Beebe, T. Kanesue, M. Okamura, J. Ritter and R. Scott, Rev. Sci. Instrum. 91, 023320 (2020)

[14] B. N. Chichkov, C. Momma, S. Nolte, F. von Alvensleben and A. Tunnermann, Appl. Phys. A 63, 109-115 (1996)

[15] A. Bayerle, M. J. Deuzeman, S. van der Heijden, D. Kurilovich, T. de Faria Pinto, A. Stodolna, S. Witte, K. S. E. Eikema, W. Ubachs, R. Hoekstra, and O. O. Versolato, Plasma Sources Sci. Technol. **27** 045001 (2018)

[16] M. J. Deuzeman, A. S. Stodolna, E. E. B. Leerssen, A. Antoncecchi, N. Spook, T. Kleijntjens, J. Versluis, S. Witte, K. S. E. Eikema, W. Ubachs, R. Hoekstra, and O. O. Versolato, Journal of Applied Physics 121, 103301 (2017)

[17] W. Bauder, R. C. Pardo, F. G. Kondev, S. Kondrashev, C. Nair, O. Nusair, T. Palchan, R. Scott, D. Seweryniak, R. Vondrasek, P. Collon, M. Paul, Nuclear Instruments and Methods in Physics Research B 361, pp. 465-470 (2015)

[18] B. Jaeggi, B. Neuenschwander, M. Schmid, M. Muralt, J. Zuercher, U. Hunziker, Physics Procedia 12, pp. 164-171 (2011)